



High-temperature oxidation of proximal basaltic pyroclasts, 1886 Tarawera, New Zealand

Hannah C. Moore¹ · Rebecca J. Carey¹ · Bruce F. Houghton² · Martin Jutzeler¹ · James D. L. White³

Received: 20 October 2021 / Accepted: 25 February 2022 / Published online: 5 April 2022
© The Author(s) 2022

Abstract

Microlite crystallization in erupting basalt can occur in the conduit, in flight, or in situ after deposition. Distinguishing the products of primary versus secondary (post-fragmentation) crystallization can be challenging in near-vent environments, but is vital for interpreting shallow conduit conditions from pyroclast textures. Here, we examine pyroclasts of the 1886 basaltic Plinian eruption of Tarawera volcano, New Zealand, to assess the roles of primary versus secondary crystallization of microlites. Lapilli and ash were selected from (a) an ultra-proximal section (T47), < 100 m from vent, which is dominated by pyroclasts derived from the Plinian jet and column margin, and (b) a medial fall deposit section (T43), 2.5 km from the fissure, which contains products from the umbrella cloud. Strong contrasts in pyroclast groundmass crystallinities exist between sections, from near-holocrystalline (90–97% void-free corrected; VFC) in T47 pyroclasts to highly crystalline (77–83% VFC) in T43 pyroclasts. Subhedral-euhedral Fe–Ti microlites (< 3 μm) are ubiquitous and abundant in T47 pyroclasts, whereas they are virtually absent in T43 pyroclasts. Olivine is present in both T47 and T43 pyroclasts but evidence of its subsolidus transformation is only seen in T47 clasts, whereas in T43 clasts olivine is fresh. Near-complete crystallization of the groundmass and subsolidus transformation of olivine in the ultraproximal T47 clasts are evidence that post-depositional modification of primary pyroclast textures occurred in ultra-proximal environments at Tarawera as a response to high residual temperatures and oxidizing conditions, aided by short transport times of relatively coarse ejecta at high accumulation rates, likely supplemented by intense vent-derived heat. Ultra-proximal basaltic eruption products can continue to crystallize after deposition and are thus unlikely to be faithful indicators of shallow conduit magmatic processes; we recommend the use of medial and distal products instead.

Keywords Eruption · Basalt · Groundmass crystallinity · Microlites · Fe–Ti oxide · Post-depositional crystallization

Editorial responsibility: C. Cimarelli

This paper constitutes part of a topical collection:

What pyroclasts can tell us

✉ Hannah C. Moore
Hannah.Moore@utas.edu.au

¹ Centre for Ore Deposit and Earth Sciences, School of Natural Sciences, University of Tasmania, Hobart, Tasmania 7001, Australia

² Department of Geology and Geophysics, University of Hawai'i, Honolulu, HI 96822, USA

³ Geology Department, University of Otago, Dunedin 9054, New Zealand

Introduction

Basaltic Plinian volcanic eruptions are rare but can be unexpected and therefore hazardous events, and hence better understanding the triggering mechanisms and conduit processes involved is critical for hazard assessment (e.g., Coltelli et al. 1998; Houghton et al. 2004a, b; Costantini et al. 2009). The proximal deposits of large Plinian explosive eruptions are only rarely preserved due to the destruction or burial of the vent area during or after the explosive phase of the eruption (e.g., Novarupta, Fierstein et al. 1997; Houghton et al. 2004a, b). An exceptionally well-preserved proximal near-vent deposit was produced from a basaltic Plinian eruption at Tarawera volcano, New Zealand, in 1886 (Sable et al. 2006b): the most recent well-documented basaltic Plinian eruption on Earth and the only one with quantitative constraints and visual

observations. In addition to the near-vent (proximal) deposits at Tarawera, the medial–distal deposits are also preserved, which enables us to examine differences in pyroclast textures with distance from the vent.

Pyroclast shapes and textures from historical basaltic Plinian eruptions represent the best source of information about eruption and fragmentation dynamics for powerful end-members (e.g., Sable et al. 2006a, b; Sable et al. 2009; Costantini et al. 2010; Bamber et al. 2020), since eye-witness observations of such eruptions are rare and conduits and deeper sub-volcanic systems are not accessible. Pyroclasts can be generally categorized into two groups (White and Houghton 2006): (1) juvenile, derived from the fragmentation of newly erupted magma, or (2) lithic, derived from entrainment of the country rock hosting the volcanic system. Microtextures of juvenile pyroclasts reflect one or more of the following processes: (a) magma ascent to fragmentation, (b) cooling during transport, (c) post-depositional modification, and (d) recycling while in a hot state. Most work focuses on (a) (e.g., Sparks 1978; Houghton and Wilson 1989; Polacci et al. 2003; Cimarelli et al. 2010; Arzilli et al. 2019; Di Genova et al. 2020; Heinrich et al. 2020; Taddeucci et al. 2021), with fewer studies addressing (b) and (c) (e.g., Sparks and Wright 1979; Yamagishi and Feebrey 1994; Tait et al. 1998; Hort and Gardner 2000; Capaccioni and Cuccoli 2005; Del Moro et al. 2013; Moitra et al. 2018), and (d) (e.g., D’Oriano et al. 2013, 2014; Deardorff and Cashman 2017).

Close to the vent, especially within the crater, newly deposited coarse pyroclasts may continue to cool slowly or even be reheated. While the pyroclast exteriors are likely quenched during transport, if the interiors are above the temperature of glass transition, they may experience post-depositional textural modifications. The degree of textural modifications is controlled by the temperature of the clasts and the rate of heat loss. Rapid deposition of juvenile pyroclasts at temperatures above the glass transition may permit: (1) microlite nucleation and growth (e.g., Szramek et al. 2010), (2) bubble nucleation, growth, collapse, and deformation (e.g., Rothery et al. 2007), (3) subsolidus transformation of minerals, e.g., Fe–Ti oxide and olivine (e.g., Haggerty and Baker 1967; Del Moro et al. 2013), and (4) ductile flattening, annealing and welding of pyroclasts (e.g., Giordano et al. 2005; Sumner et al. 2005; Bertagnini et al. 2011). Slow cooling of pyroclasts in situ is promoted by (i) larger clasts, as they cool more slowly, (ii) short transport times in the atmosphere, (iii) enhanced heat retention of the deposit due to high accumulation rates, and (iv) heat from the nearby vent, adjacent volcanic jets, or high temperature volatiles streaming through the vent and deposits (e.g., Sparks and Wright 1979; Sumner 1998; Sumner and Branney 2002; Woodcock et al. 2016). Pyroclasts deposited far from the vent, i.e., in medial and distal locations, undergo rapid cooling in the plume and are generally cold at deposition (Thomas and Sparks 1992). Groundmass textures of products

from medial and distal deposits thus best preserve conduit processes, whereas near-vent deposits may be more equivocal.

Recycling of hot juvenile pyroclasts in the vent can also modify primary volcanic textures (e.g., Rosseel et al. 2006; D’Oriano et al. 2013, 2014; Lefebvre et al. 2013; Schipper and White 2016; Deardorff and Cashman 2017). Textures associated with recycling or reheating of pyroclasts in an intra-crater setting (e.g., at Stromboli) include changes in external morphology, extensive crystallization of the groundmass, precipitation of oxides on external clast surfaces, and subsolidus transformation of mineral phases (D’Oriano et al. 2013, 2014). Oxidized basaltic pyroclasts display a red or brown discoloration, chiefly controlled by the growth or alteration of iron-oxide mineral species (Houghton and Carey 2015). The significance of textures formed by high-temperature oxidation of basaltic pyroclastic deposits in the ultra-proximal environment has not previously, to our knowledge, been investigated in detail.

In this study, we focus on the 1886 Tarawera eruption to investigate post-depositional modifications of primary pyroclastic textures. The 1886 Tarawera eruption deposits are useful for this investigation due to the excellent preservation and comparability of the ultraproximal and medial deposits. This allows us to investigate textural differences between pyroclasts that experienced long transport times and rapid cooling, versus pyroclasts which experienced extended timescales for cooling at high temperatures in the deposit adjacent to the vent. We examine in detail the microlite, olivine and vesicle textures of lapilli and ash samples from unwelded horizons, comparing products from a proximal section dominated by ballistic and small clasts (median diameter -2.4 to -4.7Φ for Plinian phase deposits; Carey et al. 2007) sedimented from jet margins and the lower convective column (Carey et al. 2007; Sable et al. 2009; T47), and a medial fall deposit section with ash and lapilli sedimented from the Plinian umbrella cloud (Sable et al. 2009; T43). We identify characteristics of 1886 pyroclasts that are attributed to post-depositional high-temperature oxidation.

Eruption chronology

The eruption of Tarawera began early on June 10, 1886, when an 8-km-long fissure opened along Mt Tarawera in the northeast, and basaltic magma was subsequently explosively erupted from over 50 discrete vents over a period of approximately 4 h. Visual observations of the eruption and its timing were recorded as eye-witness accounts that provide quantitative constraints on the dynamics and impacts of the eruption (Smith 1886a, b; Smith 1886a, b; Williams 1887). A detailed chronology was inferred from these accounts (Cole 1970; Nairn 1979; Keam 1988, 2016; Houghton and Wilson 1998). At $\sim 12:30$ a.m. on June 10 (all times are local), sustained ground shaking began (Smith 1886a, b). Earthquake activity

increased in intensity until the eruption began at ~ 1:30 a.m. from a vent within the Wahanga dome, in the northeastern portion of Mt Tarawera (Keam 1988) (Fig. 1a). By 2:30 a.m., an 8-km-long line of craters hosted erupting vents along the Mt Tarawera segment (Williams 1887). Eyewitness accounts reported that these vents were in sustained eruption forming a convective column more than 10 km high (Williams 1887). At ~ 3:30 a.m., the fissure propagated across the Rotomahana swamps, lakes and geothermal system. Interaction of the basaltic magma with ground, surface and geothermal waters produced a 10–13-km-high eruption column that deposited wet fall and surge deposits, the “Rotomahana Mud” (Cole 1970). The entire 17-km rift, including the Rotomahana and Waimangu segments, was in eruption until ~ 6:00 a.m. (Hutton 1887; Keam 2016), with some weak explosions persisting for years at Waimangu (Cole 1970).

Eruption deposits

The first detailed physical volcanology study of the 1886 deposits was carried out by Walker et al. (1984), who defined five proximal units on crater walls within 400 m of the inferred vents, and mapped these units across Mt Tarawera. Houghton and Wilson (1998) later re-grouped the five units into three: phreatomagmatic Unit 1, magmatic Unit 2/3, and phreatomagmatic Unit 4/5. These three units can be followed along the walls through the entire 8-km-long fissure segment. The proximal deposits now exposed on the crater wall were not directly exposed to the vent or eruption jet during the climactic phase of the eruption because late-stage phreatomagmatic activity subsequently excavated earlier deposits while widening the craters (Sable et al. 2006b) (Fig. 2).

Houghton and Wilson (1998) correlated the medial–distal fall deposit (Figs. 1a and 3) with proximal Unit 2/3 deposits in the crater walls at Mt Tarawera (Figs. 1 and 2) and proposed that intense eruptive activity from the northeastern fissure segment was sustained for most of the eruption’s duration. We define the current crater walls, about 50–150 m from the original vents, as ‘ultra-proximal’ (Fig. 1). The ultra-proximal deposits vary between black and red in color along the Mt Tarawera portion of the fissure (Fig. 1b) (Walker et al. 1984; Houghton and Wilson 1998; Sable et al. 2006b; Carey et al. 2007). Walker et al. (1984) attributed color differences to changes in eruption behavior and intensity. The color of the deposits was later suggested to have more complex origins, because color changes transect both bedding and individual clasts (Fig. 1c) (Houghton and Wilson 1998).

Sable et al. (2006b) separated Unit 2/3 deposits on the crater walls into tephra “packages” of contrasting dispersal (Fig. 2). Linear half-thicknesses ($t_{1/2}$) of individual tephra packages were determined, with a higher $t_{1/2}$ equating to

greater heights of particle release and hence derived from vents in higher intensity eruption; lower $t_{1/2}$ equates to lower particle-release heights, from vents erupting at lower intensity. Field measurements give $t_{1/2}$ values ranging from < 20 to ~ 280 m, which suggest that different vents erupted with variable intensities over the course of the eruption (Sable et al. 2006b). Four of the thirteen major craters produced widespread packages with $t_{1/2} > 150$ m, most likely representing the vents erupting at high intensity that fed the convecting column and Plinian umbrella cloud (F, H, J, L, Fig. 1; Sable et al. 2006b).

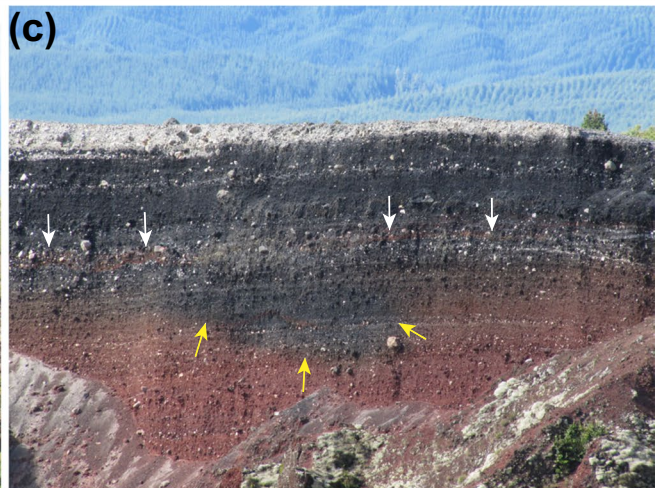
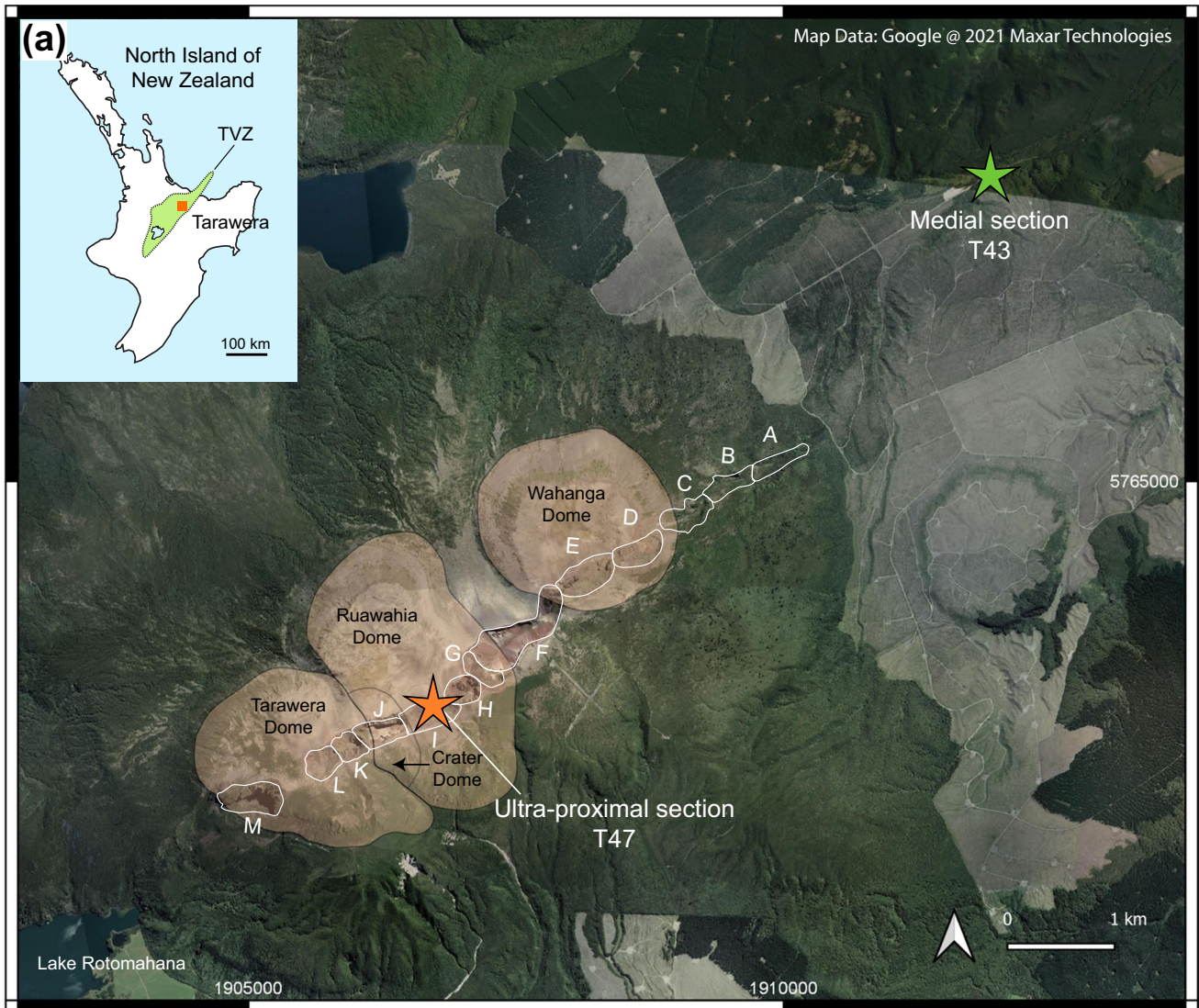
Alternating non-welded and welded beds are observed within Unit 2/3 (Carey et al. 2007; Sable et al. 2009). Welding varies laterally and vertically within packages, both abruptly and gradationally and is strongest in locally dispersed packages, although zones of strong welding do occur in a few very widespread packages (Sable et al. 2006b). Similar degrees of welding found in packages with $t_{1/2}$ between 5 and 100 m demonstrate the complexity associated with simultaneous deposition of clasts from multiple vents of contrasting intensity (Sable et al. 2006b). Some non-welded packages have accumulation rates higher than suggested minimum rates for welding (e.g., Sparks and Wright 1979), justified by such packages either (i) including clasts with longer transport times in the upper levels of the plume; and/or (ii) having a high content of cold lithic wall rock; and/or (iii) having some degree of magma–water interaction (Sable et al. 2006b). Clast flattening is also observed in some beds, although these are often the largest clasts (e.g., bombs; Carey et al. 2007).

The 1886 medial–distal deposits comprise only material sedimented from the high parts of the Plinian plume, and are dominated by pyroclasts erupted from vents within the craters F, H, J, and L (Sable et al. 2006b). Admixed ash from erupting vents in the Rotomahana portion of the fissure (from 3:30 a.m. to 6:00 a.m. on June 10) can be found in the upper layers of the 1886 deposits. This ash is called the ‘Rotomahana Mud’ and is a distinctive gray, fine-grained, lithic-rich ash, which commonly coats larger clasts. The temporal relationship between the Rotomahana Mud and the Tarawera lapilli varies across the footprint of the combined deposit (Carey et al. 2007; Sable et al. 2009; Rowe et al. 2021).

Methods

Sample collection and density measurements

Two sampling locations were selected to represent markedly different pyroclast sedimentation histories and post-depositional thermal environments (Fig. 1a). We used previously collected samples from an ultra-proximal section



adjacent to Crater I (T47) that features widespread packages ($t_{1/2} > 80$ m), and a medial section (T43) 2.5 km to the NE of the Tarawera fissure (Fig. 1a) (Carey et al. 2007; Sable

et al. 2009). This collection includes (a) 72 samples of ~100 16–32 mm juvenile clasts (lapilli) from T47, and (b) 11 samples of ~100 16–32 mm lapilli from T43. These clasts were

Fig. 1 (a) Google Earth image of Mt Tarawera in the Taupo Volcanic Zone (TVZ) (orange square on inset map) with outlines of craters A–M, (after Carey et al. 2007); sampling locations in colored stars; 1314 AD Kaharoa lava domes in pale orange. Coordinate reference system: EPSG: 2193 New Zealand Transverse Mercator 2000. (b) Red and black ultra-proximal deposits; coloration is not confined to beds or clasts of specific types or sizes, indicating that red oxidation is likely largely a post-depositional process. (c) Zoom in of (b). Yellow arrows point to a horizon of red-colored deposits with overlying black deposits. White arrows point to thin layer of red deposits underlain and overlain by black deposits

sampled from narrow vertical intervals no more than 10 cm thick.

The degree of welding varies through the T47 section (Carey et al. 2007). All lapilli were sampled from non-welded beds, although adjacent beds were welded (Fig. 2). T47- ρ 22 is from a non-welded bed which lies on top of a bed containing flattened bombs. T47- ρ 20 and T47- ρ 19 are from alternating welded and non-welded beds containing flattened bombs. T47- ρ 12 is from a non-welded bed with flattened bombs.

Although deposits range in color from red to black through the ultra-proximal deposits, all T47 clasts analyzed are red and undeformed. The T43 deposits are black to gray, and all T43 pyroclasts analyzed are black.

The density of each lapilli was measured following Houghton and Wilson (1989). Bulk vesicularity was calculated using a bulk dense rock equivalent (DRE) density of 2900 kg m^{-3} , (Houghton and Wilson 1989). Density histograms for studied samples are shown in Figs. 2 and 3. Five modal density lapilli from beds in Unit 2/3 were selected for microtextural analysis from each section to represent the bulk of the erupted magma. In some cases, where there are broad principal modes, lapilli were taken from multiple bins (e.g., T43- ρ 08; Fig. 4).

Three samples of ash (G16 from ρ 22), in the size range $250 \text{ }\mu\text{m}$ –1 mm, were selected for textural analysis from Unit 2/3 at T47. Ash was embedded within resin then polished for Backscattered Electron (BSE) imaging.

Vesicle analysis

Selected lapilli were thin sectioned and nested images were generated using the FEI MLA650 scanning electron microscope (SEM) for low magnifications and the Hitachi SU-70 field emission analytical SEM for higher magnifications. See Online Resource 1 and Fig. S1 for more details on imaging strategy. We used Adobe Photoshop CS6 software to select vesicles from crystals and groundmass. See Online Resource 2 for more details on image processing. Binarized images were analyzed using the FIJI software package to calculate individual vesicle areas. Two-dimensional size distributions (number per unit area, N_A) were then converted

to volume distributions (number per volume, N_V) using the stereological method of Sahagian and Proussevitch (1998). The cumulative number density (N_V total) referenced to the matrix of the clast records the rate and timing of nucleation of vesicles during the rise of a body of magma. See Adams et al. (2006); Shea et al. (2010); Stovall et al. (2011); Parcheta et al. (2013) for further details on the method. All vesicularity data are provided in Table 1.

Groundmass crystallinity

Groundmass crystallinity (area %) was calculated from high magnification BSE images, at $250 \text{ }\mu\text{m}$ horizontal field width and a scale factor of 10,240 px/mm. Such high magnifications were used to image groundmass crystallinity and to exclude phenocrysts (generally $> 100 \text{ }\mu\text{m}$), xenoliths, and large vesicles. Mineral phases, glass and vesicles were then manually selected using Photoshop with the aid of element maps. The abundance of each phase (crystals, matrix glass and vesicles) was measured using the FIJI software package. The crystallinity % of each groundmass phase was calculated on a vesicle-free basis. All crystallinity data are provided in Table 2.

We measured the area % of plagioclase, olivine, pyroxene, and Fe–Ti oxide microlites ($< 100 \text{ }\mu\text{m}$). Area % of pyroxene and groundmass glass in T43 is only approximate as BSE grayscales are indistinguishable using our image analysis methods. See Online Resource 3 for more details on methods used to gather crystal area % data.

Crystal size distributions and crystal number densities could not be calculated due to the difficulty in outlining individual crystals in the extremely crystal-rich groundmass made of overlapping crystals, especially in pyroclasts from the ultra-proximal deposits.

Results

Juvenile clast density and bulk vesicularity

For this study, T47 ρ samples were chosen from beds within the most widespread packages and were therefore most likely dominated by clasts erupted from high intensity vents (following Sable et al. 2006a, b). The T43 ρ samples were chosen such that they represent Unit 2/3 below the major influx of Rotomahana Mud. T47 and T43 ρ samples are relatively similar in terms of their density ranges (800 to 2000 kg m^{-3} on average; Figs. 2 and 3) and their modal densities (1000 – 1200 kg m^{-3} on average), although T43 has a higher standard deviation (240 – 320 kg m^{-3}) compared to T47 (190 – 230 kg m^{-3}) due to the tails of dense clasts. Almost all selected T43 ρ samples have multiple modes, versus only one weakly bi-modal sample from T47 (Fig. 4).

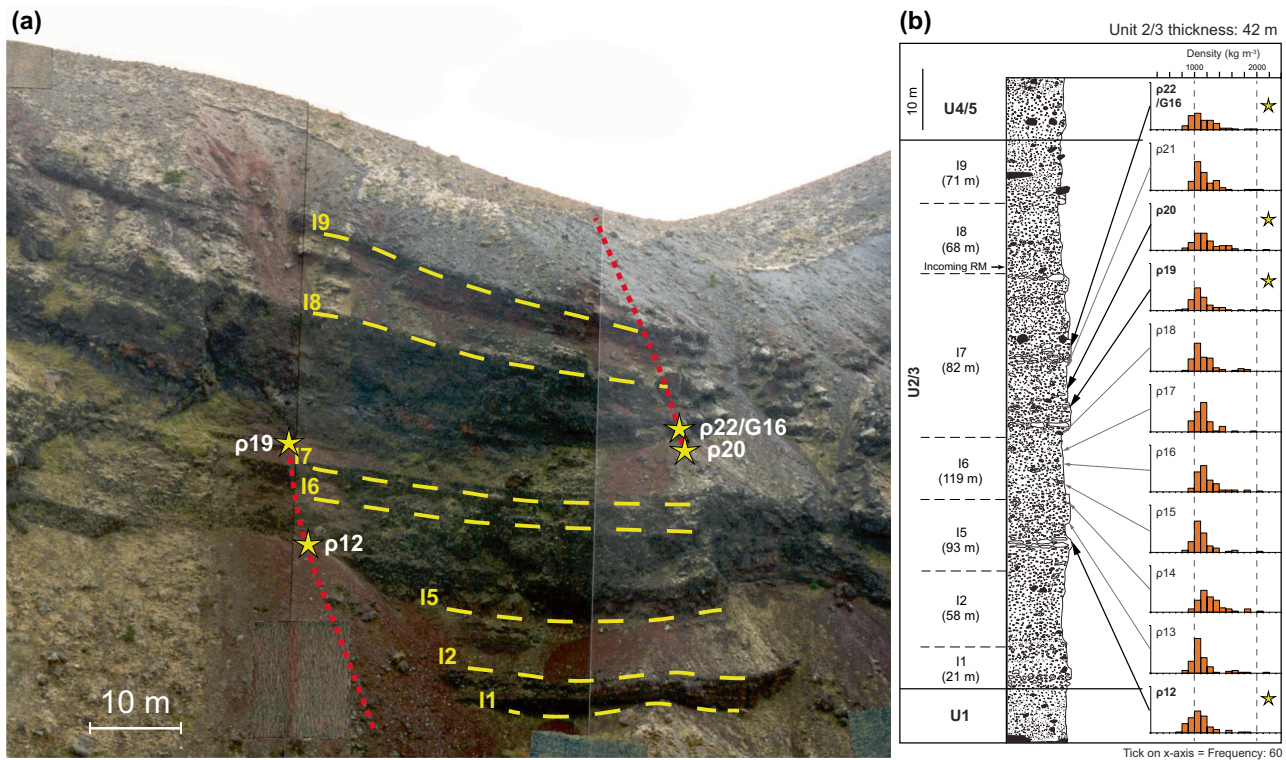


Fig. 2 (a) Ultra-proximal (T47) section with overlain sketch of the package geometry. Welded beds protrude out from cliff face. Red dashed lines represent logged and sampled stratigraphy. Yellow stars represent location of samples selected for density measurements. (b) Composite stratigraphic sections for ultra-proximal section (T47) after Carey et al. (2007) and Sable et al. (2009), with juvenile clast density histograms by Sable et al. (2009). Vertical gray dashed lines are drawn through 1000 and 2000 kg m^{-3} . Open symbols are basal-

tic juvenile clasts, black symbols are rhyolite lithic clasts and dashed symbols are mud-coated juvenile lapilli. Samples used for textural analysis in this study are indicated with yellow stars, bold sample names and thick arrows. Packages defined by Sable et al. (2006b) are indicated by crater letter (I) and number. The corresponding thinning half distance ($t_{1/2}$) for each package is given below the package label in parenthesis. 'RM' is Rotomahana Mud

Selected clast vesicularity ranges are slightly higher for T47 clasts (59.8–63.8%) than T43 clasts (56.3–61.8%).

Vesicles

2D observations of vesicle textures from both lapilli and ash

The vesicle textures in T47 lapilli are nearly identical to those in T43 (Table 1). Lapilli from both sections contain highly irregular, complex and polylobate-shaped vesicles with a wide range of sizes (mean size interval from selected lapilli are 0.02 to 2.5 mm; Fig. 5). Vesicles < 0.1 mm are generally more circular or lobate. Vesicle number densities fall in a narrow range of $2\text{--}5 \times 10^6 \text{ cm}^{-3}$ (with one outlier at $5 \times 10^5 \text{ cm}^{-3}$) for the five T47 lapilli and $1\text{--}6 \times 10^6 \text{ cm}^{-3}$ for the five T43 lapilli (Table 1), identical to vesicle number densities calculated by Sable et al. (2009). In both T47 and T43 lapilli, vesicles are typically smaller at the rims and larger in the cores, although this feature is more evident in

T47 lapilli. The vesicle size distributions of T47 and T43 lapilli are broadly the same (Fig. S2).

Vesicle sizes in the ash particles from T47 ultra-proximal ejecta are extremely similar to those of its lapilli, although larger vesicles (> 0.3 mm) are limited in the ash. The T47 ash contains circular and lobate vesicles identical in size to the lower range of the T47 lapilli (mean size interval of 0.02 to 0.3 mm).

A subpopulation of small ($< 30 \mu\text{m}$) voids are common in all Tarawera lapilli (Fig. 5i,j,k,l), although their abundance generally correlates with groundmass crystallinity. We refer to these features as voids because they have separate size-frequency distributions decoupled from the vesicle population $> 30 \mu\text{m}$ (Fig. S2) and often contrasting morphologies and dispersal habits from larger populations of vesicles.

Although only modal density clasts from T47 and T43 samples were studied in detail, we also briefly examined textures of dense and vesicular clasts from the investigated samples. Dense and vesicular clasts from each sample have similar number densities to the modal clasts, but dense clasts

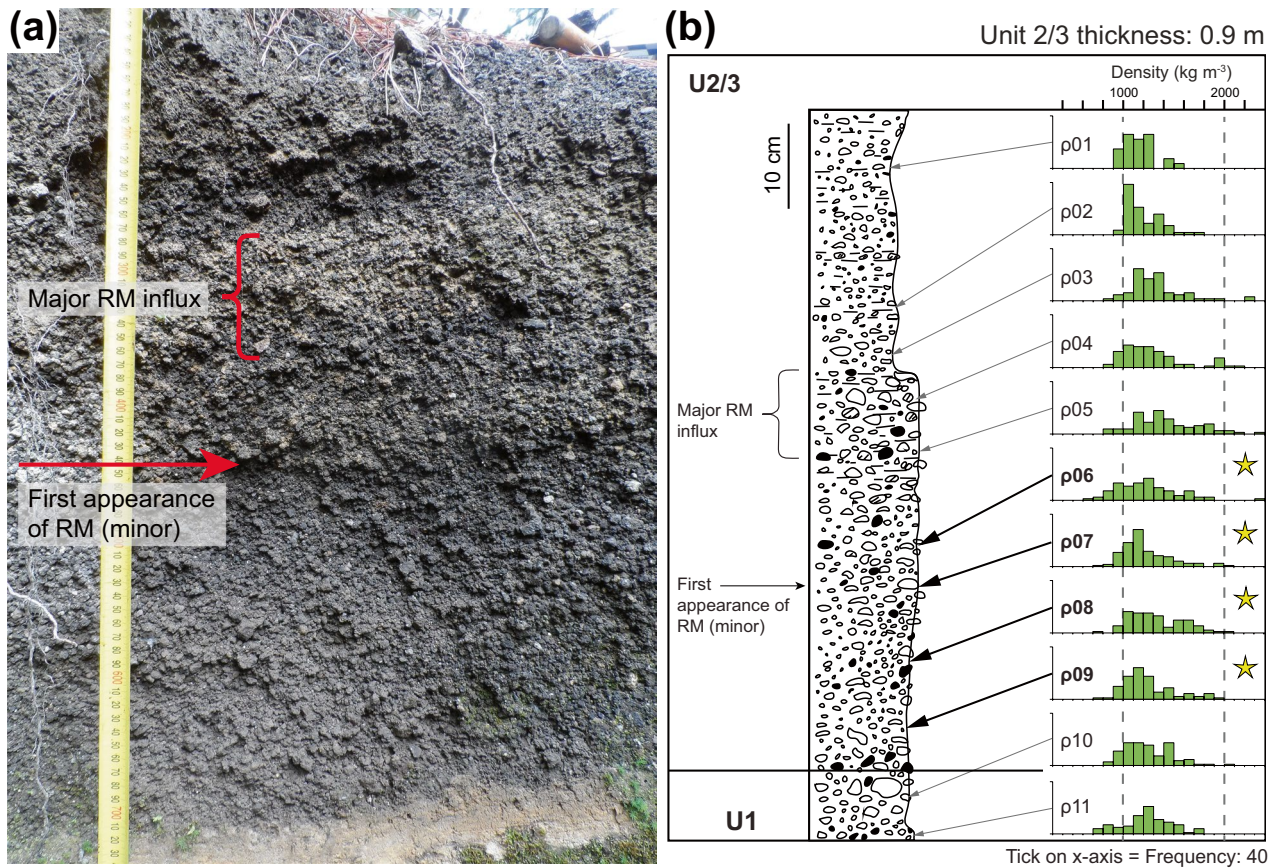


Fig. 3 (a) Stratigraphic characteristics of northeastern 1886 medial deposits including Rotomahana Mud (RM). (b) Composite stratigraphic sections for Plinian deposits from medial section (T43), with juvenile clast density histograms by Sable et al. (2009). Vertical gray dashed lines are drawn through 1000 and 2000 kg m⁻³. Open symbols

are basaltic juvenile clasts, black symbols are rhyolite lithic clasts and dashed symbols are mud-coated juvenile lapilli. Samples used for textural analysis in this study are indicated with yellow stars, bold sample names and thick arrows. ‘RM’ is Rotomahana Mud

have comparatively small, widely spaced vesicles and vesicular clasts have larger and more polylobate vesicles.

The roughness of vesicle walls correlates weakly with groundmass crystallinity. Clasts with near-holocrystalline groundmass (T47) have highly irregular and angular vesicle walls due to the protrusions of microlites toward the inner portions of vesicles (Fig. 5i,j), whereas clasts with lower groundmass crystallinities (T43) have smoother inner walls with fewer protrusions of microlites (e.g., Fig. 5k,l).

To summarize, in general, the vesicle textures in T47 pyroclasts are nearly identical to those in T43, but there are subtle qualitative differences related to protrusions of microlites into vesicles that are not captured in quantitative data.

Microlites

Groundmass textures of the 10 modal density juvenile lapilli (5 from T47, 5 from T43; Fig. 4) and 3 ash samples across two size intervals (0 and 2 ϕ) from T47-G16 (equivalent stratigraphic height to ρ22) have been qualitatively and quantitatively

characterized (Table 2). We group the groundmass textures into two categories (near-holocrystalline and highly crystalline), based on the areal ratio of microlites to glass (Table 2).

The total groundmass crystallinities of modal lapilli contrast markedly between T47 and T43 (Figs. 6, 7, 8, Table 2): T47 lapilli are near-holocrystalline (90–96 area %, e.g., Fig. 6a,b) while T43 lapilli have a relatively lower crystallinity but are still highly crystalline (77–83 area %, e.g., Fig. 7). Although only modal density lapilli were chosen to be studied, we observed that dense and vesicular clasts have identical crystallinities to modal clasts. Based on examination of many other grains in BSE, there is some subtle variability in groundmass texture of the products from each investigated sample, but we believe that the textures in selected clasts are representative of the bulk of the magma. Phenocryst content is very low (<0.5 vol.% of the clasts; Sable et al. 2009) with little variability throughout each sample.

The groundmass of the lapilli and ash in both sections consists of differing proportions of microlites of plagioclase, pyroxene and olivine (Figs. 6 and 7; Table 2). Residual glass is present in varying proportions in T43

Fig. 4 Clast density distribution histograms for Unit 2/3 of the ultra-proximal (T47) samples and medial (T43) samples used in this study, drawn in stratigraphical order (see Fig. 2). Vertical gray dashed lines are drawn through 1000 and 2000 kg m⁻³. Stars indicate modal juvenile clasts selected for textural analysis. Each clast is labeled with its respective vesicle number density (N_v; cm⁻³), modal density (Mode; kg m⁻³) and vesicularity (vesic; vol.%). Density data summary for each sample is shown on the right side of each histogram. St. dev.: Standard deviation. Min and max represent the minimum and maximum density, respectively

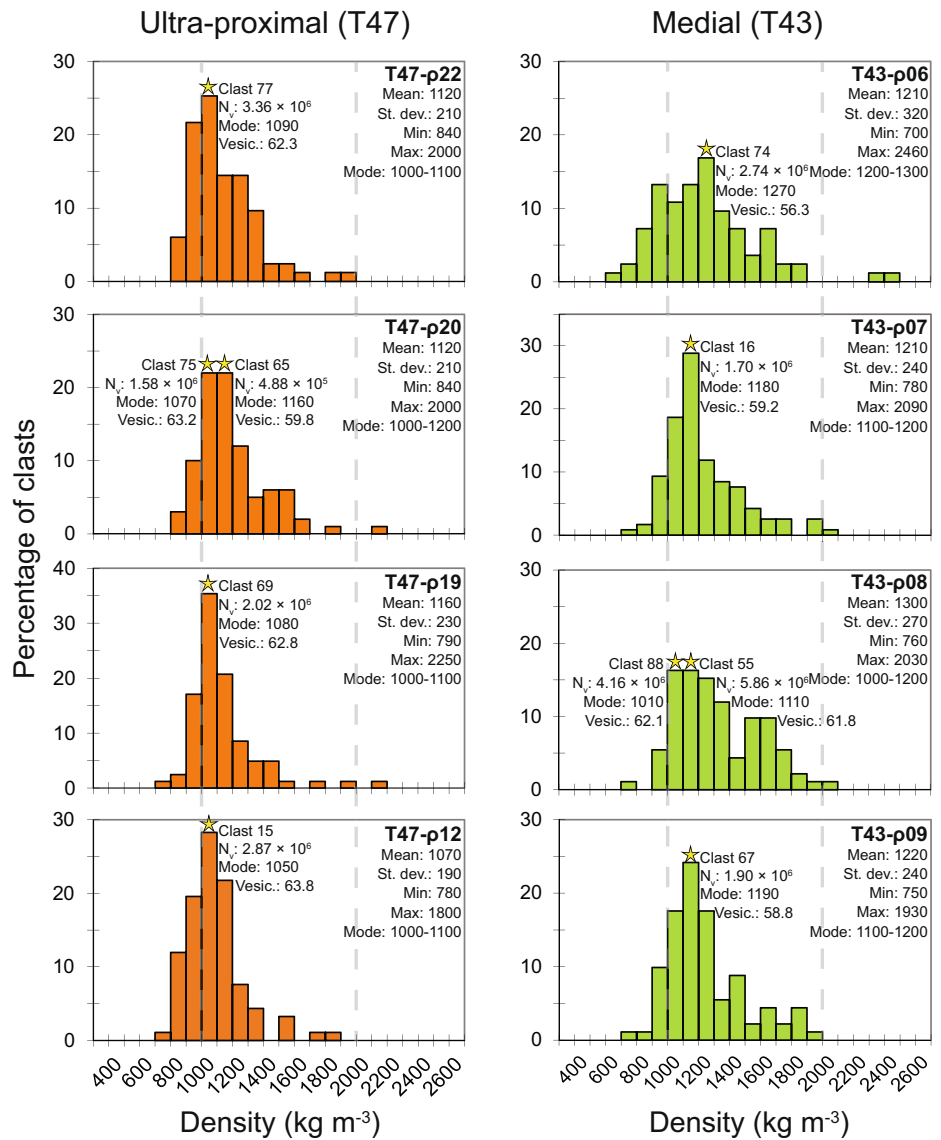


Table 1 Vesicularity data for selected 1886 Tarawera modal density lapilli. N_A is number of vesicles per unit area and N_v is number of vesicles per unit of volume. A width cutoff of 10 μm was used for vesicle number densities, and a width cutoff of 2 μm was used for number densities of voids < 30 μm

Section	Clast	Density (g cm ⁻³)	Bulk vesicularity (vol.%)	N _A (cm ⁻²)	N _v (cm ⁻³)	Number of analyzed vesicles included	N _v < 30 μm (cm ⁻³)
Ultra-proximal (T47)	ρ12-15	1.05	63.8	8.40 × 10 ³	2.87 × 10 ⁶	581	1.86 × 10 ⁸
	ρ19-69	1.08	62.8	6.35 × 10 ³	2.02 × 10 ⁶	553	2.71 × 10 ⁸
	ρ20-65	1.16	59.8	1.29 × 10 ³	4.88 × 10 ⁵	463	1.96 × 10 ⁸
	ρ20-75	1.07	63.2	4.66 × 10 ³	1.58 × 10 ⁶	614	2.40 × 10 ⁸
	ρ22-77	1.09	62.3	7.18 × 10 ³	3.36 × 10 ⁶	684	4.23 × 10 ⁸
Medial (T43)	ρ06-74	1.27	56.3	7.44 × 10 ³	2.74 × 10 ⁶	488	2.51 × 10 ⁸
	ρ07-16	1.18	59.2	4.27 × 10 ³	1.70 × 10 ⁶	961	3.36 × 10 ⁸
	ρ08-55	1.11	61.8	1.31 × 10 ⁴	5.86 × 10 ⁶	579	1.96 × 10 ⁸
	ρ08-88	1.01	62.1	9.47 × 10 ³	4.16 × 10 ⁶	400	2.65 × 10 ⁸
	ρ09-67	1.19	58.8	5.21 × 10 ³	1.90 × 10 ⁶	1049	3.31 × 10 ⁸

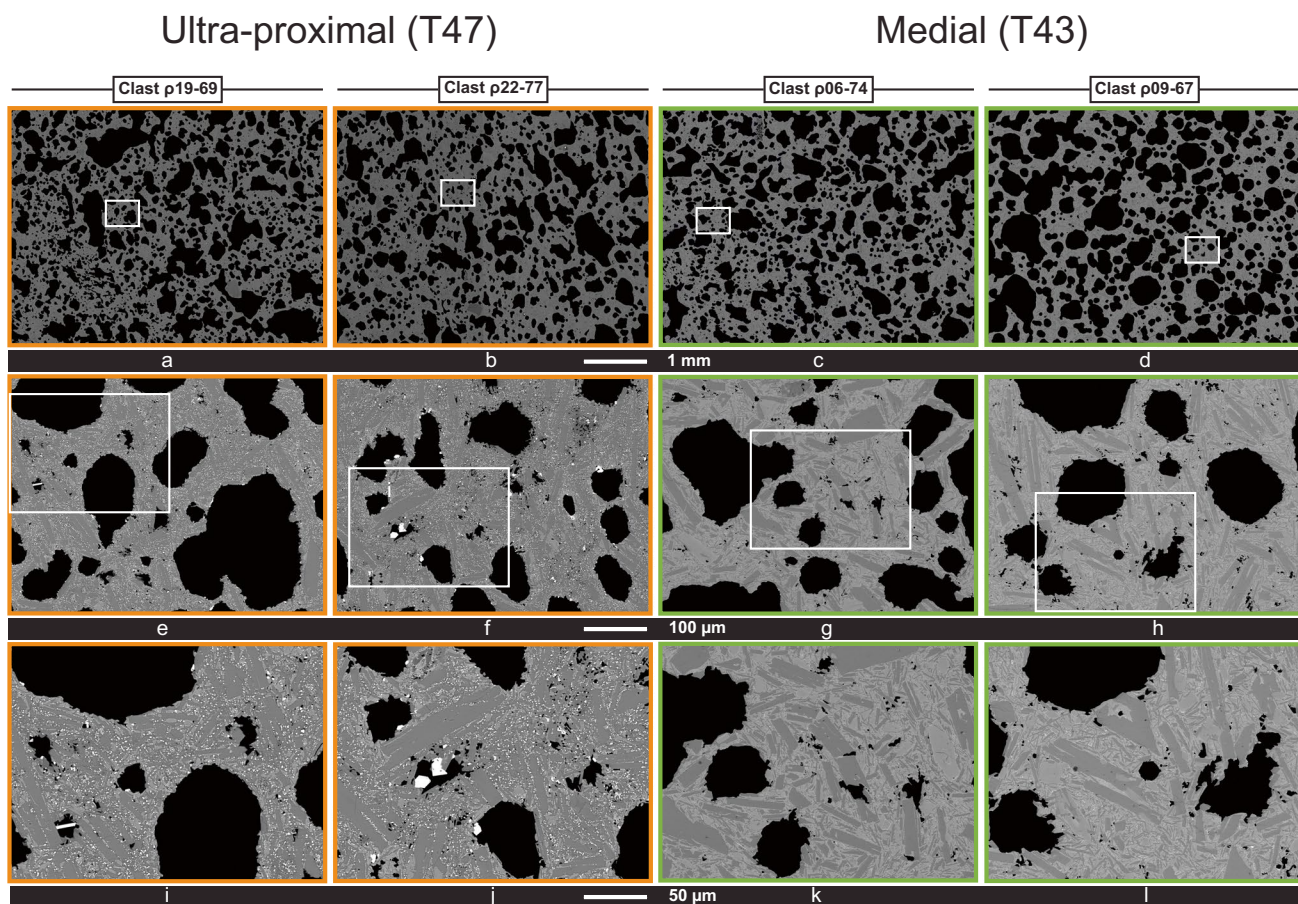


Fig. 5 BSE images showing groundmass textures of lapilli-sized clasts taken from Unit 2/3 of the ultra-proximal section (T47; two left orange columns) and the medial section (T43; two right green columns). Vesicle textures are similar between the sections, although

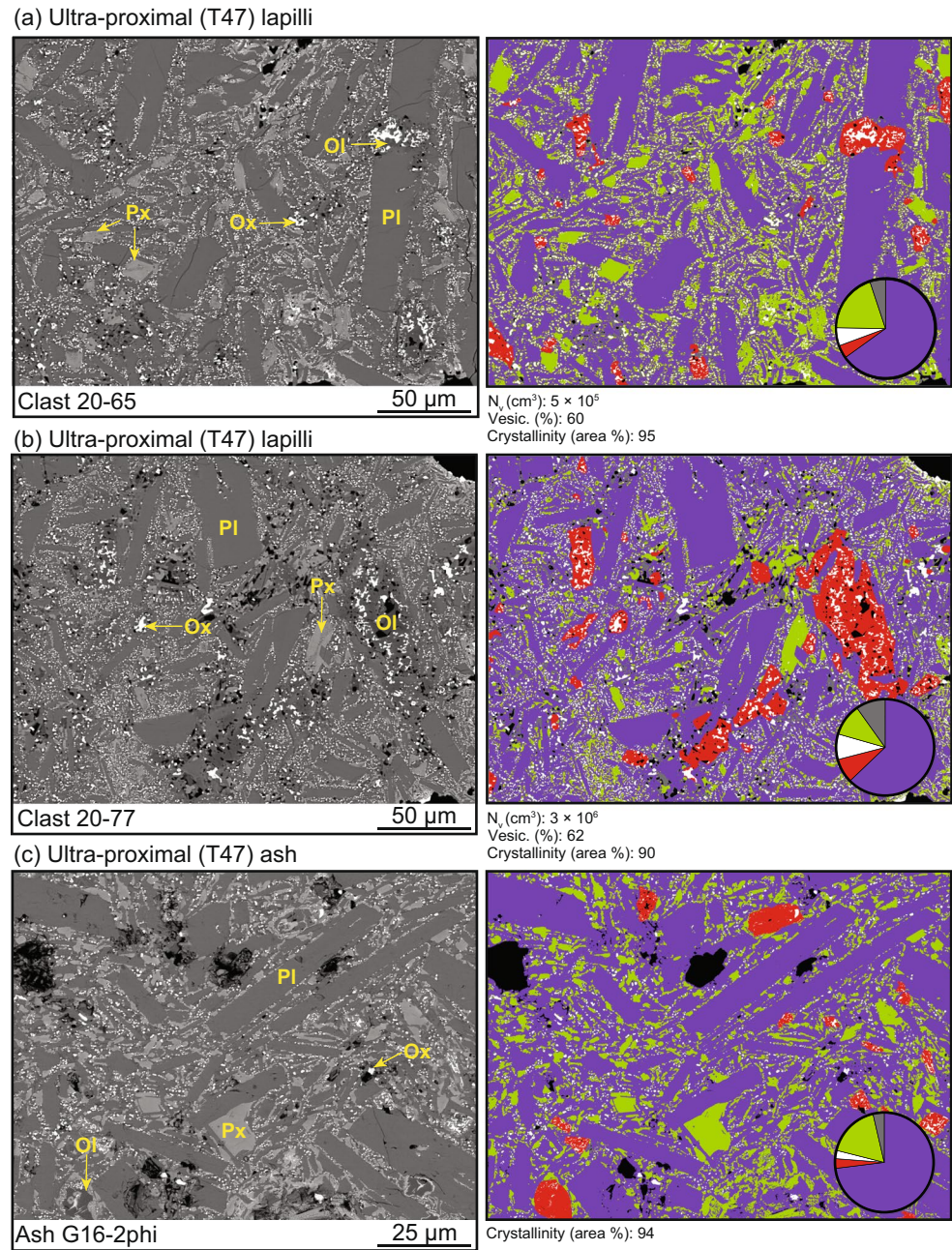
there are more microlite protrusions on vesicle inner walls in T47 compared to T43. Vesicles in black, groundmass in gray, and microlites in gray and white

Table 2 Summary of groundmass measurements obtained from Tarawera samples using BSE images at a field of view of 250 µm (area 47,000² µm). ϕ is the crystallinity. Vesicle area % has been

removed from phase area % calculations. Area % of pyroxene and glass in T43 is only approximate as BSE grayscales are indistinguishable

Section	Clast	Sample type	Apparent ϕ	ϕ (area %)	Groundmass (area %)				
					Glass	Plagioclase	Olivine	Pyroxene	Oxide
Ultra-proximal (T47)	ρ 12-15	lapilli	Holocrystalline	96	4	66	2	22	5
	ρ 19-69	lapilli	Holocrystalline	91	9	59	7	19	7
	ρ 20-65	lapilli	Holocrystalline	95	5	65	4	20	6
	ρ 20-75	lapilli	Holocrystalline	90	10	66	5	11	8
	ρ 22-77	lapilli	Holocrystalline	90	10	63	8	11	8
	G16-0 ϕ -1	ash	Holocrystalline	97	3	78	3	10	6
	G16-0 ϕ -2	ash	Holocrystalline	94	6	70	3	14	8
	G16-2 ϕ -3	ash	Holocrystalline	96	4	73	3	17	3
Medial (T43)	ρ 06-74	lapilli	High	83	17	58	7	17	<1
	ρ 07-16	lapilli	High	80	20	56	4	20	<1
	ρ 08-55	lapilli	High	77	23	54	6	16	<1
	ρ 08-88	lapilli	High	78	22	56	7	16	<1
	ρ 09-67	lapilli	High	80	20	59	5	15	<1

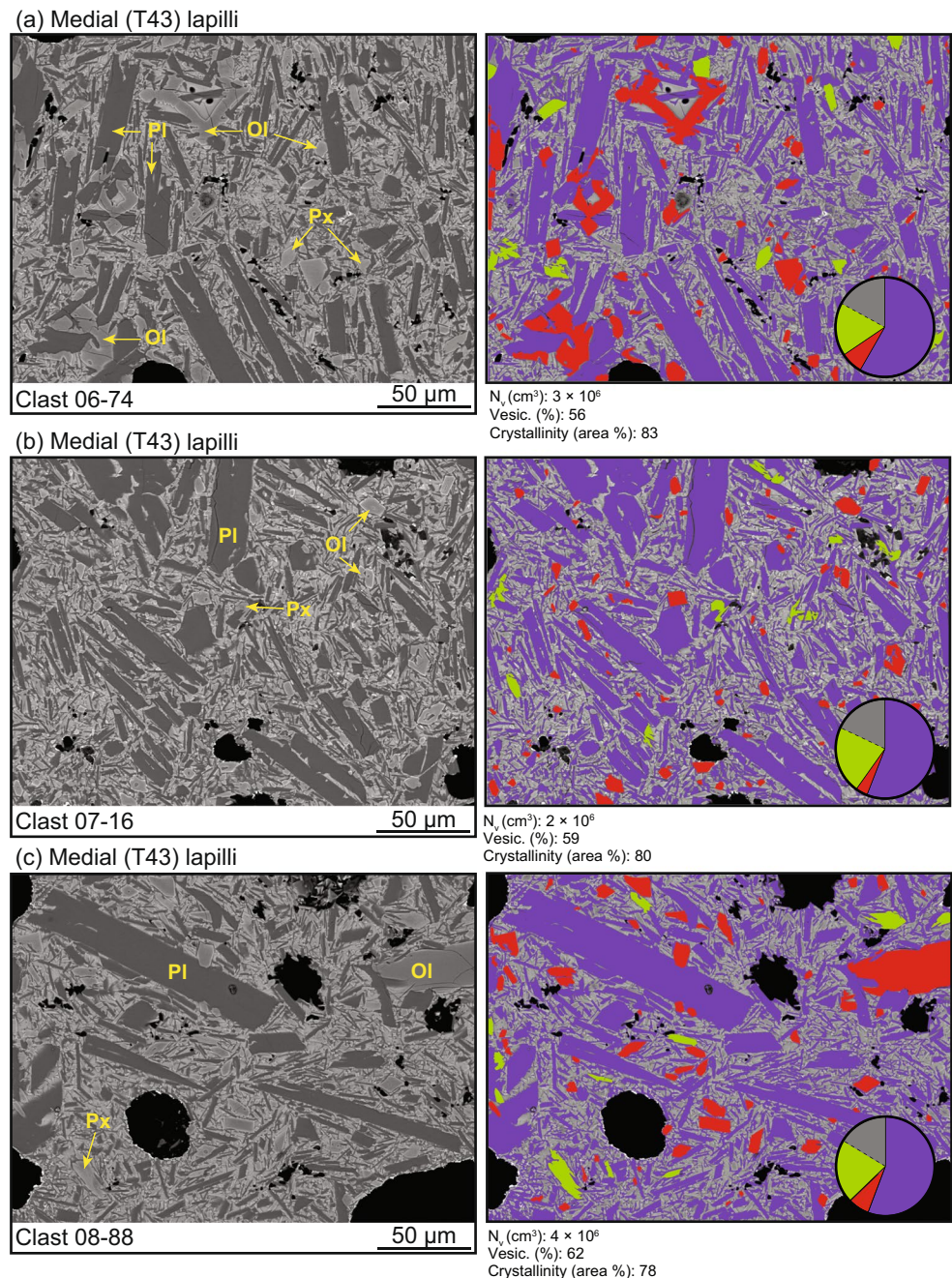
Fig. 6 BSE images of lapilli (a, b) and ash (c) from T47 (left columns), false-colored in Photoshop according to different phases (right columns). Note the near-holocrystalline groundmass crystallinity with very little glass and presence of euhedral Fe–Ti oxide microlites. Purple: plagioclase feldspar, red: olivine, green: pyroxene, white: oxide, black: vesicles, gray: glass. Each clast is labeled with its respective number density (N_v), vesicularity (vesic.) and crystallinity (Tables 1 and 2). Vesicles have been removed from area % calculations for each pie chart



but is virtually absent in T47. Fe–Ti oxide microlites of all sizes are only present in T47 lapilli and ash and are virtually absent in T43. Microlites are randomly distributed through the groundmass in both T47 and T43 ash and lapilli, and are chiefly randomly oriented, except near vesicles, where long axes are generally parallel to the vesicle margins. There are no rim-to-core variations in microlite crystallinity in either T47 or T43 pyroclasts. Size ranges of crystal phases between T47 and T43 are generally similar regardless of pyroclast size (e.g., ash versus lapilli for T47).

Across the suite of T47 lapilli, the area % of different microlite phases can vary by up to 11%: 59–66% for plagioclase; 2–8% for olivine; 11–22% for pyroxene; and 5–8% for Fe–Ti oxide (Table 2). Plagioclase is typically tabular or acicular and pyroxenes are prismatic. The groundmasses of all T47 lapilli contain equant subhedral-euhedral Fe–Ti oxide ($< 3 \mu\text{m}$) grains irregularly distributed between the coarser microlites (Fig. 8, left column). Coarser oxides (3–40 μm) are also present in low abundance, particularly inside vesicles and ‘void’ spaces (e.g., Fig. 5, left columns).

Fig. 7 BSE images of lapilli from T43 (left columns), false-colored in Photoshop according to different phases (right columns). Note the high groundmass crystallinity with absence of Fe–Ti oxides. Purple: plagioclase feldspar, red: olivine, green: pyroxene, black: vesicles. Gray in false-colored images corresponds to undifferentiated glass and small pyroxene microlites. Each clast is labeled with its respective vesicle number density (N_v), vesicularity (vesic.) and crystallinity (Tables 1 and 2). Vesicles have been removed from area % calculations for each pie chart. Dashed line on pie chart corresponds to an approximation of the ratio between pyroxene and glass



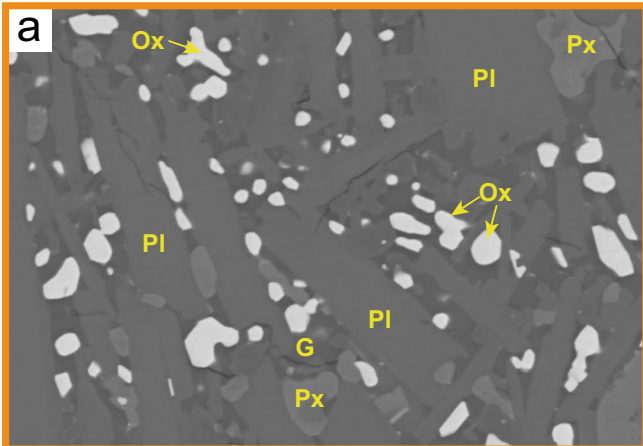
T47-G16 ash shows the same near-holocrystalline groundmass (94–97 area %, e.g., Fig. 6c) to T47-p22 lapilli (from the same stratigraphic height) and other T47 lapilli (Table 2). T47-G16 ash also shows similar microlite abundances, sizes, habits and morphologies to T47-p22 lapilli and other T47 lapilli (Table 2 and Fig. 6c). Like p22 lapilli and other lapilli, microlites are randomly distributed throughout the groundmass in G16 ash. Size ranges of phases in G16 ash are similar to T47 lapilli, although Fe–Ti oxides < 3 μm in G16 ash are slightly smaller in size compared to T47-p22

lapilli and other lapilli (Figs. 6c and 8). The larger Fe–Ti oxides (> 3 μm) are not as abundant in T47-G16 ash compared to T47-p22 lapilli and other lapilli.

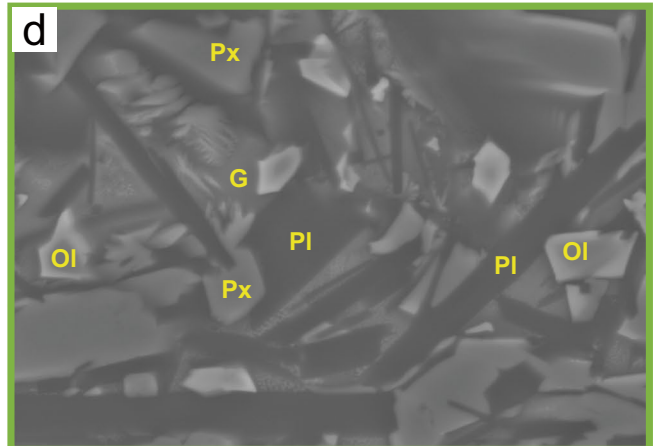
In T43 lapilli, the area % of microlite phases varies by up to 5%: 54–59% for plagioclase; 4–7% for olivine, approx. 15–20% for pyroxene; and < 1% for Fe–Ti oxide (Table 2). The coarser oxides (3 μm –40 μm) observed in T47 ejecta are absent in T43 lapilli (Figs. 7 and 9) and equant Fe–Ti oxide microlites (< 3 μm) are very rare (< 1%) and only occur with dendritic habits.

Ultra-proximal (T47)

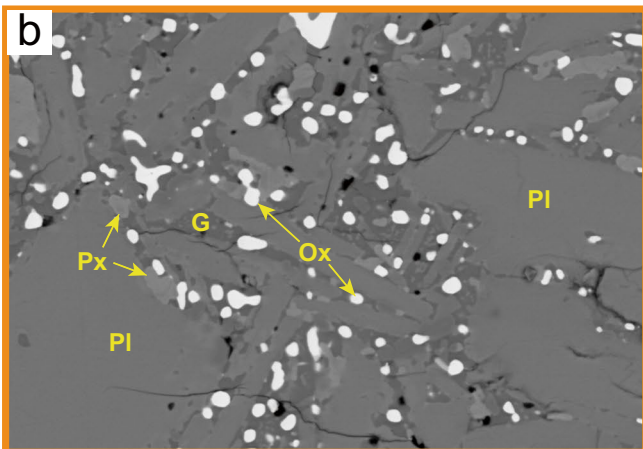
Medial (T43)



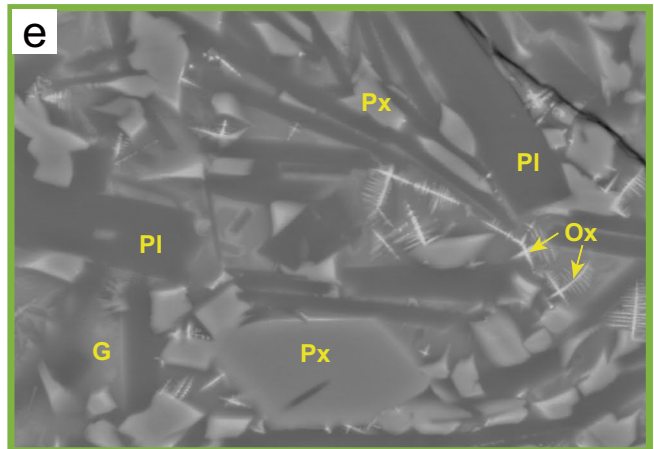
Clast 19-69



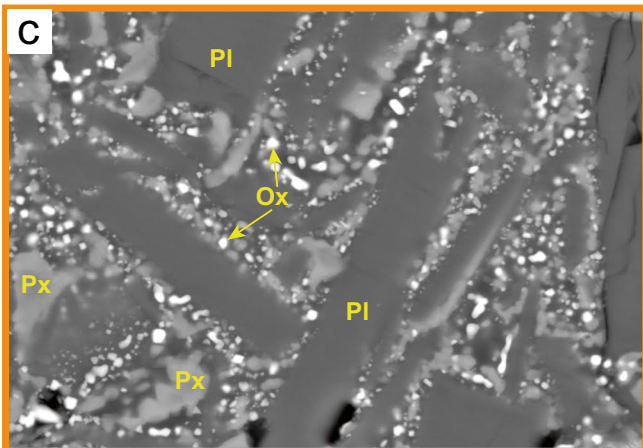
Clast 07-16



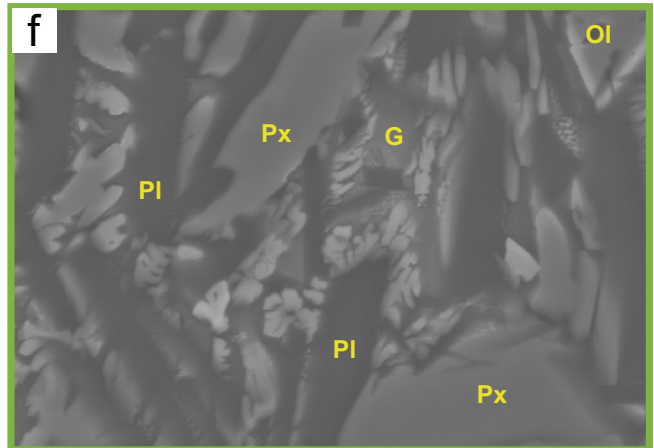
Clast 20-65



Clast 08-88



Ash-G16-2phi



Clast 09-67

Fig. 8 High magnification BSE images from (a, b) ultra-proximal (T47) lapilli, (c) ultra-proximal (T47) ash particle, and (d–f) medial (T43) lapilli. T47 pyroclasts contain subhedral-euhedral Fe–Ti oxides of varying sizes and abundances. T43 pyroclasts contain very few

Fe–Ti oxides, only occurring in dendritic habits. Pl: Plagioclase, Px: pyroxene, Ol: olivine; Ox: Fe–Ti oxide, G: groundmass glass. Scale bar: 5 µm

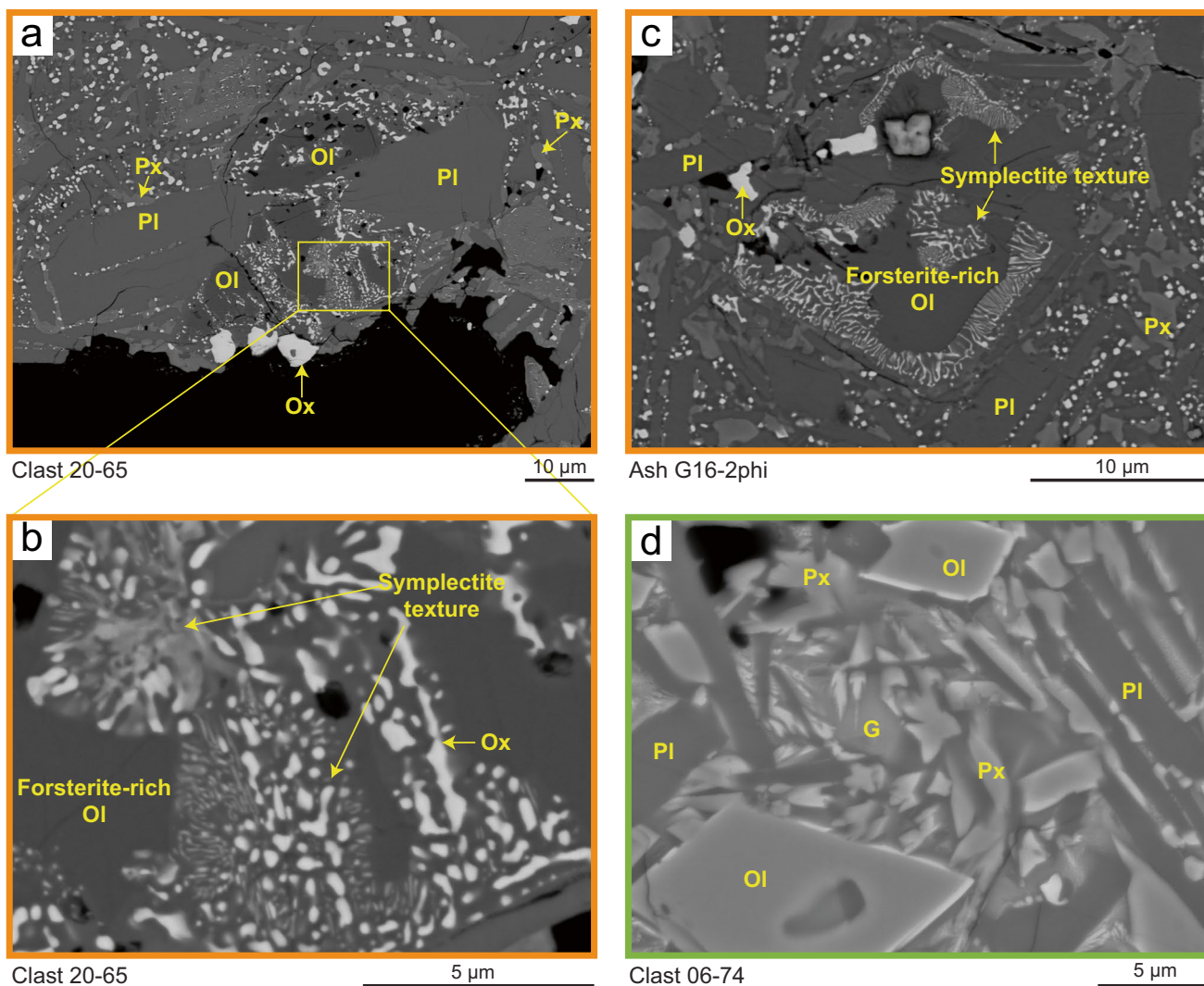


Fig. 9 BSE images of olivine textures from (a, b) ultra-proximal (T47) lapilli, (c) ultra-proximal ash (T47), and (d) medial (T43) lapilli. Olivine crystals in T47 pyroclasts display symplectitic texture, whereas olivine crystals in T43 pyroclasts remain fresh. Orange bor-

ders enclose T47 pyroclasts, green border encloses a T43 pyroclast. Pl: Plagioclase, Px: pyroxene, Ox: Fe oxide, G: groundmass glass, Ol: olivine

Olivine subsolidus transformation

Olivine is rare in all studied clasts ($\leq 8\%$). In clasts from T47, olivine crystals show varying degrees of oxidation, reflecting subsolidus transformations (e.g., Haggerty and Baker 1967; Del Moro et al. 2013; D’Oriano et al. 2014). All olivine crystals observed (~ 250) in T47 clasts displayed subsolidus transformations (e.g., Fig. 9a,b,c; Online Resource 5). In contrast, all T43 olivines are fresh (e.g., Fig. 9d). In BSE images of T47 pyroclasts, olivines commonly show exsolution of Fe oxides as symplectitic intergrowths or patches, either along crystal rims, along fracture

lines, or throughout the crystals (Fig. 9a,b,c). Although minerals associated with the subsolidus transformation of olivine are too small to be analyzed on the SEM by Energy Dispersive Spectroscopy (SEM-EDS) or by Electron Probe Micro Analysis (EPMA), we have tentatively identified the minerals by comparison of microtextures with those reported from experimental (Haggerty and Baker 1967) and other studies of olivine subsolidus transformation (Del Moro et al. 2013) and with results from element mapping (Online Resource 6). The Fe oxide minerals are probably titanium-poor Mg-ferrite or magnetite phases in which the Mg content is strictly related to the availability of ferrous

iron in the system (i.e., strictly related to the fO_2 conditions which control the subsolidus transformation). Mg-ferrite is the product of substitution of Fe^{2+} by Mg^{2+} during olivine oxidation (Del Moro et al. 2013). The mineral intergrown with the Mg-ferrite is likely forsterite, which, together with orthopyroxene, is a common product of subsolidus transformation of olivine (Haggerty and Baker 1967).

Discussion

Groundmass and olivine textures

Pyroclasts deposited in the ultra-proximal environment (e.g., T47) are particularly subject to post-depositional textural changes because they are coarse (up to bomb-sized), experienced short transport times, and have accumulated quickly in a hot environment close to the erupting vents. Welded horizons within the T47 strata (Fig. 3) indicate that the deposits could reach a bulk temperature in excess of that of glass transition, permitting annealing, ductile deformation and welding processes. For high temperature basaltic magmas, post-fragmentation textural changes in lapilli and larger pyroclasts are difficult to avoid without extremely rapid cooling rates (Gardner et al. 1996).

The differences between juvenile pyroclasts from the ultra-proximal versus the medial Unit 2/3 deposits include (1) groundmass crystallinity, which is higher in T47 lapilli than in T43 lapilli; (2) the presence or absence of Fe–Ti oxide microlites, which are abundant in T47 and virtually absent in T43 pyroclasts; (3) oxide morphology, with T47 pyroclasts containing larger numbers of euhedral Fe–Ti grains $< 3 \mu\text{m}$ than T43 ones, which contain much fewer $< 0.1 \mu\text{m}$ dendritic Fe–Ti microlites (Fig. 8); and (4) presence or absence of subsolidus olivine transformation, with all T47 olivine crystals exhibiting subsolidus transformation in the form of symplectitic (i.e., exsolution) intergrowth textures, whereas olivine is pristine in T43 pyroclasts (Fig. 9).

Pyroclasts with the highest microlite abundance are commonly inferred to represent cooler and slower ascending or stalled magmas along the margins of the upper conduit compared to their lower crystallinity counterparts inferred to ascend along the central axis of the conduit (e.g., Taddeucci et al. 2004; Sable et al. 2006a; Cimarelli et al. 2010). Such contrasts in crystal textures are commonly coupled with differences in vesicle textures; however, they are not coupled in our samples. Interpreting the near-holocrySTALLINE (90–97%) T47 lapilli and ash as representative of syn-eruptive conduit conditions is not plausible because (i) the magma would have been too crystalline to flow (e.g., Caricchi et al. 2007), and (ii) a significant volume of this microlite-rich magma would need to be erupted at very high magma discharge

rates and replenished quickly throughout this high intensity phase. This scenario is highly unlikely. We suggest that the discrepancy of groundmass crystallinity between T47 and T43 pyroclasts is due to post-depositional crystallization of dominantly plagioclase and Fe–Ti oxides, due to hot emplacement and slow cooling rates of the ultra-proximal deposits.

Post-depositional crystallization in T47 pyroclasts is also indicated by subhedral-euhedral Fe–Ti oxides $< 3 \mu\text{m}$ which are completely absent in T43 clasts. Primary subhedral-euhedral morphologies of Fe–Ti oxides are often considered indicative of steady growth from low to moderate undercooling conditions (Hammer et al. 1999). These features have also, however, been attributed to magma oxidation before fragmentation due to convective circulation that allowed exposure to the atmosphere before recirculation in the upper part of the conduit, or due to recycling of juvenile pyroclasts (Genareau et al. 2010; D’Oriano et al. 2013, 2014; Dearth and Cashman 2017). Convective circulation is highly unlikely due to the sustained nature of this eruption and the rapid ascent rates of the magma in the conduit (Sable et al. 2009). We suggest that the abundant and dispersed $< 3 \mu\text{m}$ Fe–Ti oxides in T47 pyroclast textures are most consistent with post-depositional crystallization, rather than recycling, because other diagnostic textures of hot-state recycling such as cored lapilli are rare to absent (D’Oriano et al. 2013, 2014; Dearth and Cashman 2017). Further, recycling is not consistent with the sustained and intense eruption style during this phase.

We propose that the ultra-proximal deposits of the 1886 Tarawera eruption were emplaced at a bulk temperature that was above or close to the glass transition, and cooled relatively slowly due to high proximal accumulation rates. Further, these deposits could have been exposed to vent-derived heat moving upward and outward through the interstitial space in the deposits. We cannot constrain the timescales required for textural modification of the T47 pyroclasts in the ultraproximal setting because the exact behavior of the bulk deposit temperature through time is unknown, and uncertainties remain regarding crystallization kinetics of Fe–Ti oxides at temperatures close to the glass transition. However, thick m-scale densely welded horizons within the T47 section certainly suggest that bulk temperatures above the glass transition could have lasted many hours. This interpretation implies that the assumption that all ultraproximal 1886 pyroclast textures represent conduit conditions at fragmentation is incorrect.

At T47, both the lapilli and ash have extremely similar groundmass textures, including evenly distributed granular Fe–Ti oxides ($< 3 \mu\text{m}$) and near-complete groundmass crystallization. The similarities between these different grainsizes are surprising given the expected differences in particle cooling rates. These textures are ubiquitous in

T47 products (approximately 100 ash particles in 0–2 Φ size range and all modal juvenile lapilli analyzed (13), see Online Resource 7). Further, lapilli and ash from the same stratigraphic horizon (T47-p22/T47-G16), have extremely similar groundmass crystallinities (Table 2). This is interesting because ash < 2 mm should have very rapid cooling rates in the atmosphere (a reasonable quench rate is 10–20 K s⁻¹; Xu and Zhang 2002) and should have been deposited cold in the ultra-proximal environment (Moitra et al. 2018). Reheating ash above the glass transition is thermally very energy intensive. There are four options to explain the similar groundmass textures between T47 ash and lapilli: (1) all the ash is secondary, derived from lapilli and bombs by abrasion during sampling and particularly sieving; (2) the ash was rapidly deposited at bulk temperatures above the glass transition such that it could continue to crystallize the groundmass; (3) the ash was re-reheated after deposition; or (4) the ash and the lapilli have the same crystallinity and primary magmatic phases, but these textures were produced in substantially different ways; the ash is the result of more efficient brittle fragmentation of highly crystallized magma at the margins of the conduit, whereas the lapilli have textures reflecting extensive post-depositional crystallization. Juvenile grain-size histograms of T47 samples presented in Carey et al. (2007) do not show an increase in the ash abundance for the fine grain-size fractions 0–2 ϕ , suggesting that the physical process of sieving is not creating artificial ash of this size. This data coupled with the qualitative observation that all ash textures are homogeneous (see Online Resources 7), suggests that (1) is highly unlikely and that textures are probably primary. There are no obvious microlite textural features in the ash to indicate whether (2), (3), or (4) is more likely, but the oxidation of olivine seen in both T47 ash and lapilli is more supportive of post-depositional textural modification (iii) and (iv) as described below.

Olivine is one of the minerals that is most effective in recording oxidizing conditions (Haggerty and Baker 1967; Del Moro et al. 2013). Subsolvus transformation of olivine has long been interpreted to reflect alteration under high temperature and oxidizing conditions (Haggerty and Baker 1967; Haggerty 1991). More recent studies have attributed similar subsolvus transformation to either (i) rapid changes in oxygen fugacity during sudden decompression of the magmatic column (Cortés et al. 2006; Knafelc et al. 2019); (ii) convective circulation of magma that is oxidized when exposed to the atmosphere during circulation (Genareau et al. 2010); (iii) exposure of deposits to high temperatures under atmospheric pressures (Del Moro et al. 2013); or (iv) recycling of pyroclasts (D’Oriano et al. 2014). Olivine crystals in both ash and lapilli from the ultra-proximal T47 locality have experienced subsolvus transformations of variable degrees, from minor symplectite intergrowth

texture on rims, to the olivine being completely unrecognizable. The olivine transformations suggest that both the ash and lapilli were heated and oxidized to varying degrees. Recent experiments on olivine oxidation suggest that rates of olivine oxidation are temperature-dependent, with nucleation of magnetite and/or hematite occurring in days to weeks at 600 °C and within minutes at 900 °C at atmospheric pressures (Knafelc et al. 2019). Ultra-proximal deposits were likely held above 600 °C for hours during and/or after the eruption ceased, allowing for mineral transformations to occur. Oxidation during rapid ascent in the conduit (i) is unlikely as we would then expect some evidence of olivine subsolvus transformation in T43 pyroclasts. Convective circulation (ii) is unlikely, as previously discussed and recycling (iv) is also unlikely because sample pyroclasts are believed to have chiefly been produced from a sustained (non-pulsatory), highly explosive eruption, and thus precludes significant recycling. Therefore, high temperatures and atmospheric conditions (iii) of the deposits is the most likely scenario.

Estimates of syn-eruptive temperatures for ultra-proximal deposits

Welding is present in multiple packages at T47 (Carey et al. 2007), although samples for this study came from non-welded beds. Welding depends on the clasts’ emplacement temperature, the accumulation rate, and the environment of deposition (e.g., solid substrate, hot pre-existing fall material, hot vent, snow, water, etc.). In welded beds adjacent to non-welded sampled beds, temperatures may have been as high as ~ 1000 °C (D’Oriano et al. 2014). Since changes in groundmass textures in basalt may occur as low as ~ 700 °C (D’Oriano et al. 2014), even the tack-welded and non-welded beds probably had sufficiently high temperatures and the oxidizing conditions needed for thermal modification because of the heat released from adjacent welding layers.

The colors of the clasts (both external surfaces and cores) at Tarawera indicate post-depositional thermal oxidation. Selected T47 lapilli and ash are ubiquitously a bright-reddish color, whereas T43 pyroclasts are black–gray in color. Reheating experiments show that reddening throughout pyroclasts probably resulted from crystallization of Fe-bearing phases due to oxidizing conditions (D’Oriano et al. 2014). The surface reddening of basalt in ash occurs within ~ 1 h at T > 700 °C in air (D’Oriano et al. 2014) and so take place rapidly during post-depositional heating. The reddish color of clasts is therefore a useful indicator for post-depositional thermal modification.

Groundmass mineral phases can indicate conditions at which the T47 pyroclast textures were modified. The micro-textures in T47 ash and lapilli indicate oxidation at a temperature sufficient to promote subhedral–euhedral growth of

Fe–Ti oxide microlites and oxidation of olivine (substituted by Fe oxide and forsterite). From experiments, D’Oriano et al. (2014) have found that oxide-rimmed minerals commonly form in reheated clasts by heterogeneous nucleation under highly oxidizing conditions and variable degrees of undercooling at temperatures of 750–1050 °C). Further constraints on clast temperatures come from experimental studies that show hematite exsolution in olivine occurs above 600 °C (in air; $P = 1$ atm) (Haggerty and Baker 1967; Khisina et al. 1998; Gualtieri et al. 2003). At temperatures above ~ 820 °C, and under oxidizing conditions, olivine reacts to form magnetite species and Mg-rich orthopyroxene (Haggerty and Baker 1967; Champness 1970; Goode 1974; Gualtieri et al. 2003). Based on the cited experimental results, we propose that the subsolidus transformations found in olivine of lapilli and ash in T47 occurred under oxidizing conditions > 600 °C. Such high temperature crystal modification at atmospheric pressures ($P = 1$ atm) is only possible with short pyroclast transport times, high deposit accumulation rates and perhaps proximity to a hot vent. Using typical basaltic glass transition temperatures of ~ 670–690 °C (Giordano et al. 2005, 2008; D’Oriano et al. 2013; Deardorff and Cashman 2017), we suggest that the T47 ash and lapilli were held above a minimum temperature of 670 °C to allow some Fe–Ti oxide crystallization of the groundmass. This temperature is consistent with the temperature estimates for subsolidus transformation of olivine from experimental studies (Haggerty and Baker 1967; Khisina et al. 1998; Gualtieri et al. 2003).

Further insight into the temperature and timing conditions for post-depositional modification of basalt products is from cooling versus reheating experiments by Burkhard (2002, 2005). The experiments suggest that plagioclase will only grow and/or nucleate as a new microlite when $T > 930$ °C. Overall, T47 clasts have a slightly higher plagioclase content (59–78 area %) compared to T43 clasts (54–59 area %), whereas pyroxene is relatively similar (11–22 area % in T47; 15–20 area % in T43). These results indicate that at least a portion of the ultra-proximal deposits were held > 930 °C for enough time for plagioclase microlites to nucleate and grow in the groundmass.

Interpretation of vesicle textures

Vesicle textures are commonly used to reconstruct magma ascent history (e.g., Cashman and Mangan 1994; Mangan and Cashman 1996; Carey et al. 2009, 2012; Shea et al. 2010). Slight differences in density distributions between 1886 ultra-proximal and medial sections are likely to reflect: (1) T47 is dominated by clasts derived from a vent erupting at high intensity, but may contain some clasts derived from adjacent vents (Sable et al. 2006b), whereas at T43

clasts were erupted in powerful fashion and all traveled to the full height of the Plinian column, but could be from up to four vent sources (e.g., Sable et al. 2006b), and (2) some T47 clasts have larger vesicles in their core than T43 clasts, which we infer reflects higher degrees of post-fragmentation bubble expansion at T47 after deposition. Vesicle size distributions (Fig. S2) are similar between T47 and T43 lapilli, but vesicle morphologies are slightly different (e.g., Fig. 5), driven by the protrusion of microlites within the vesicles in T47 ejecta that we propose formed during post-depositional crystallization. We suspect that in the ultra-proximal environment at Tarawera, post-depositional crystallization modified and overprinted primary microtextures.

Conclusions

Post-depositional thermal modification has modified the textures of pyroclasts in ultra-proximal deposits from the 1886 Tarawera eruption. The microtextures in ultraproximal ash and lapilli indicate that they were oxidized at temperatures sufficient to promote subhedral–euhedral growth of Fe–Ti microlites and subsolidus transformation of olivine, probably > 600 °C for at least tens of minutes after the eruption ceased. The higher content of plagioclase microlites in ultra-proximal pyroclasts suggests longer cooling times > 930 °C compared to pyroclasts deposited in the medial environment. Pyroclasts that were ejected higher into the volcanic plume and deposited at a significant distance from the vent did not undergo significant Fe–Ti oxide crystallization and lack subsolidus transformation of olivine. High accumulation rates of hot and coarse tephra in the ultra-proximal environment, in addition to convective heat from the vent, led to the required high post-depositional emplacement temperatures, and reduced deposit cooling rates (Fig. 10). Welding beds above and below the studied beds could have provided additional heat for late post-depositional crystallization.

To our knowledge, there have been no previous systematic studies demonstrating such textural changes from ultra-proximal to more distal settings. We suggest that post-depositional modification of groundmass textures of both ash and lapilli by retained and vent-derived heat, or by heat loss from adjacent welding beds, in the near-vent environments may be common for explosive basaltic eruption deposits globally. This is evident by the bright-reddish color of ultra-proximal deposits, e.g., 12–13 January 2011 Mt. Etna (Andronico et al. 2014); September 2008 Stromboli (D’Oriano et al. 2011); and Krafla welded layer (Calderone et al. 1990). Decompression textures of ultra-proximal basaltic eruption products are thus likely to be overprinted. We strongly recommend examining juvenile pyroclasts in medial or distal environments when available instead.

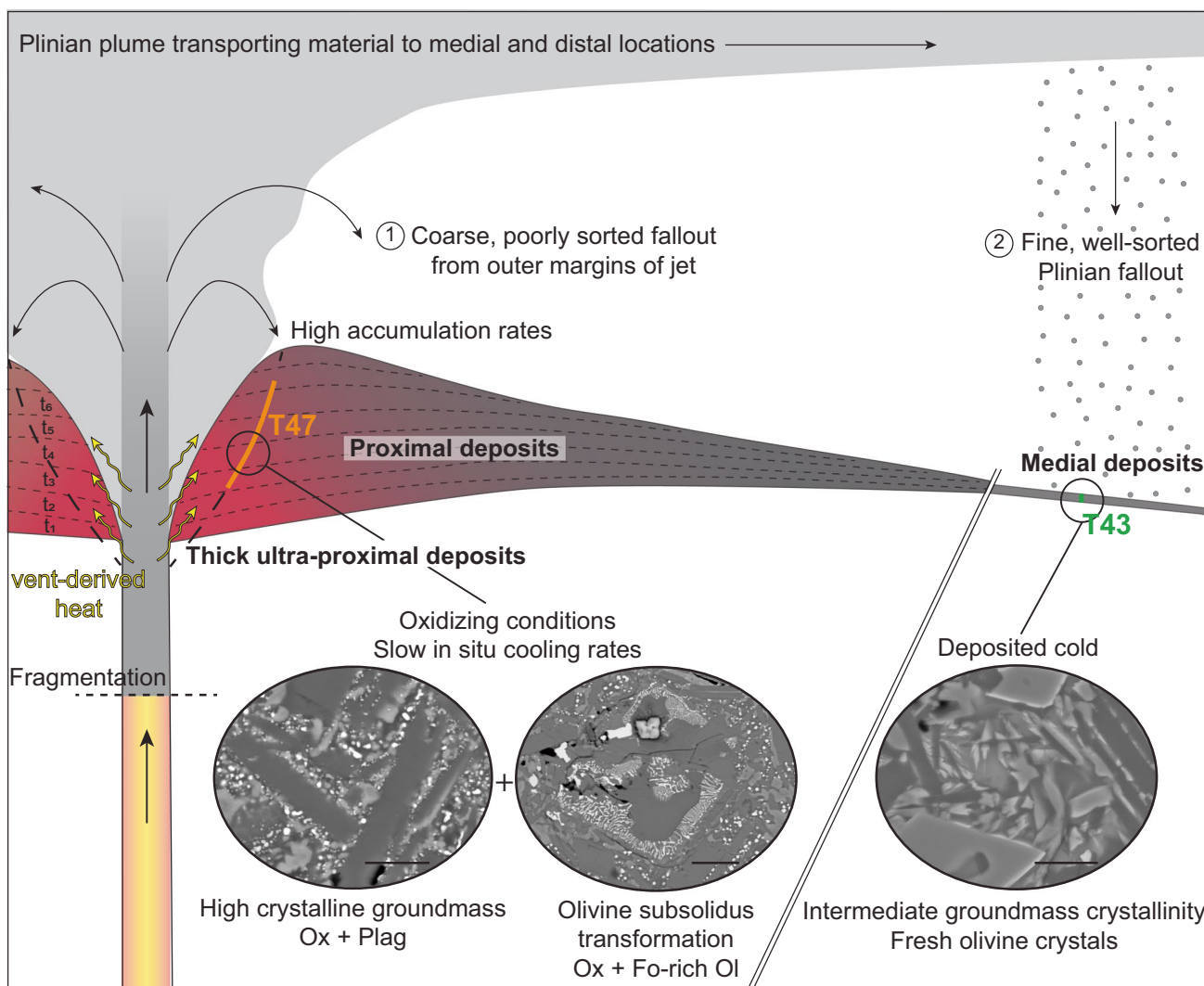


Fig. 10 Sketch (not to scale) illustrating thermal modification in the ultra-proximal area of Tarawera, versus the absence of such processes at medial sites. In the ultra-proximal environment, a combination of rapid accumulation and burial of coarse pyroclasts, convective vent-derived heat (yellow arrows), and the movement of hot gases through the deposits allowed heat retention of the rocks followed by slow cooling rates. The pyroclasts that rose well into the plume cooled

rapidly and were deposited fresh in an environment far enough away from the vent and with low enough accumulation rates so that no thermal modification processes occurred. Black dashed line through ultra-proximal deposits represents current crater walls following late-stage phreatomagmatic activity which excavated earlier deposits. Ox: Fe-oxide, Plag: Plagioclase, Ol: Olivine, Fo: Forsterite. Scale bar: 5 μm

Supplementary Information The online version contains supplementary material available at <https://doi.org/10.1007/s00445-022-01549-5>.

Acknowledgements Sandrin Feig is thanked for his support with SEM and EPMA analyses, which were carried out at the Central Science Laboratory at the University of Tasmania. We thank Wendy Cockshell for locating our requested samples from the rock store at the University of Hawaii. Thin sections were kindly prepared by Scott Wagner. Comments from two anonymous reviewers greatly improved the quality of this manuscript. Thanks to Corrado Cimarelli for handling the manuscript.

Author contributions Not applicable.

Funding Open Access funding enabled and organized by CAUL and its Member Institutions. HM’s research was funded by a University of Tasmania Graduate Research Scholarship. The research of RJC and BFH was supported by subcontracts with the Geological and Nuclear Sciences (GNS), New Zealand. JDLW’s Tarawera work was supported with a GNS Science contract.

Code availability Not applicable.

Declarations

Ethics approval and consent to participate Not applicable.

Consent for publication All authors consent to publication.

Conflict of interest The authors declare no competing interests.

Open Access This article is licensed under a Creative Commons Attribution 4.0 International License, which permits use, sharing, adaptation, distribution and reproduction in any medium or format, as long as you give appropriate credit to the original author(s) and the source, provide a link to the Creative Commons licence, and indicate if changes were made. The images or other third party material in this article are included in the article's Creative Commons licence, unless indicated otherwise in a credit line to the material. If material is not included in the article's Creative Commons licence and your intended use is not permitted by statutory regulation or exceeds the permitted use, you will need to obtain permission directly from the copyright holder. To view a copy of this licence, visit <http://creativecommons.org/licenses/by/4.0/>.

References

- Adams NK, Houghton BF, Hildreth W (2006) Abrupt transitions during sustained explosive eruptions: examples from the 1912 eruption of Novarupta, Alaska. *Bull Volcanol* 69(2):189–206. <https://doi.org/10.1007/s00445-006-0067-4>
- Andronico D, Scollo S, Cristaldi A, Lo Castro MD (2014) Representativity of incompletely sampled fall deposits in estimating eruption source parameters: a test using the 12–13 January 2011 lava fountain deposit from Mt. Etna volcano, Italy. *Bull Volcanol* 76(10):861. <https://doi.org/10.1007/s00445-014-0861-3>
- Arzilli F, La Spina G, Burton M, Polacci M, Le Gall N, Hartley M, Di Genova D, Cai B, Vo NT, Bamber E, Nonni S, Atwood R, Llewellyn E, Brooker R, Mader H, Lee P (2019) Magma fragmentation in highly explosive basaltic eruptions induced by rapid crystallization. *Nat Geosci*. <https://doi.org/10.1038/s41561-019-0468-6>
- Bamber EC, Arzilli F, Polacci M, Hartley ME, Fellowes J, Di Genova D, Chavarría D, Saballos JA, Burton MR (2020) Pre- and syn-eruptive conditions of a basaltic Plinian eruption at Masaya Volcano, Nicaragua: The Masaya Triple Layer (2.1 ka). *J Volcanol Geotherm Res* 392:106761. <https://doi.org/10.1016/j.jvolgeores.2019.106761>
- Bertagnini A, Di Roberto A, Pompilio M (2011) Paroxysmal activity at Stromboli: lessons from the past. *Bull Volcanol* 73(9):1229–1243. <https://doi.org/10.1007/s00445-011-0470-3>
- Burkhard DJ (2002) Kinetics of crystallization: example of micro-crystallization in basalt lava. *Contrib Miner Petrol* 142(6):724–737. <https://doi.org/10.1007/s00410-001-0321-x>
- Burkhard DJ (2005) Nucleation and growth rates of pyroxene, plagioclase, and Fe-Ti oxides in basalt under atmospheric conditions. *Eur J Mineral* 17(5):675–685. <https://doi.org/10.1127/0935-1221/2005/0017-0675>
- Calderone GM, Grönvold K, Oskarsson N (1990) The welded air-fall tuff layer at Krafla, northern Iceland: a composite eruption triggered by injection of basaltic magma. *J Volcanol Geoth Res* 44(3):303–314. [https://doi.org/10.1016/0377-0273\(90\)90024-A](https://doi.org/10.1016/0377-0273(90)90024-A)
- Capaccioni B, Cuccoli F (2005) Spatter and welded air fall deposits generated by fire-fountaining eruptions: cooling of pyroclasts during transport and deposition. *J Volcanol Geoth Res* 145(3):263–280. <https://doi.org/10.1016/j.jvolgeores.2005.02.001>
- Carey RJ, Houghton BF, Sable JE, Wilson CJN (2007) Contrasting grain size and componentry in complex proximal deposits of the 1886 Tarawera basaltic Plinian eruption. *Bull Volcanol* 69(8):903–926. <https://doi.org/10.1007/s00445-007-0117-6>
- Carey R, Houghton B, Thordarson T (2009) Abrupt shifts between wet and dry phases of the 1875 eruption of Askja Volcano: microscopic evidence for macroscopic dynamics. *J Volcanol Geoth Res* 184(3–4):256–270. <https://doi.org/10.1016/j.jvolgeores.2009.04.003>
- Carey RJ, Manga M, Degruyter W, Swanson D, Houghton B, Orr T, Patrick M (2012) Externally triggered renewed bubble nucleation in basaltic magma: the 12 October 2008 eruption at Halema'uma'u Overlook vent, Kilauea, Hawai'i, USA. *J Geophys Res: Solid Earth* 117(B11202). <https://doi.org/10.1029/2012j.b009496>
- Caricchi L, Burlini L, Ulmer P, Gerya T, Vassalli M, Papale P (2007) Non-Newtonian rheology of crystal-bearing magmas and implications for magma ascent dynamics. *Earth Planet Sci Lett* 264(3):402–419. <https://doi.org/10.1016/j.epsl.2007.09.032>
- Cashman KV, Mangan MT (1994) Physical aspects of magmatic degassing II Constraints on vesiculation processes from textural studies of eruptive products. In: Carroll MR, Holloway JR (eds) *Volatiles in Magmas*. Mineralogical Soc Amer, Chantilly, pp 447–478
- Champness PE (1970) Nucleation and growth of iron oxides in olivines, (Mg, Fe)₂SiO₄. *Mineral Mag* 37(291):790–800. <https://doi.org/10.1180/minmag.1970.037.291.05>
- Cimarelli C, Di Traglia F, Taddeucci J (2010) Basaltic scoria textures from a zoned conduit as precursors to violent Strombolian activity. *Geology* 38(5):439–442. <https://doi.org/10.1130/g30720.1>
- Cole JW (1970) Structure and eruptive history of the Tarawera Volcanic Complex. *NZ J Geol Geophys* 13(4):879–902. <https://doi.org/10.1080/00288306.1970.10418208>
- Coltelli M, Del Carlo P, Vezzoli L (1998) Discovery of a Plinian basaltic eruption of Roman age at Etna volcano, Italy. *Geology* 26(12). [https://doi.org/10.1130/0091-7613\(1998\)026](https://doi.org/10.1130/0091-7613(1998)026)
- Cortés JA, Wilson M, Condliffe E, Francalanci L (2006) The occurrence of forsterite and highly oxidizing conditions in basaltic lavas from Stromboli Volcano, Italy. *J Petrol* 47(7):1345–1373. <https://doi.org/10.1093/petrology/egl012>
- Costantini L, Bonadonna C, Houghton BF, Wehrmann H (2009) New physical characterization of the Fontana Lapilli basaltic Plinian eruption, Nicaragua. *Bull Volcanol* 71(3):337–355. <https://doi.org/10.1007/s00445-008-0227-9>
- Costantini L, Houghton BF, Bonadonna C (2010) Constraints on eruption dynamics of basaltic explosive activity derived from chemical and microtextural study: The example of the Fontana Lapilli Plinian eruption, Nicaragua. *J Volcanol Geotherm Res* 189(3–4):207–224. <https://doi.org/10.1016/j.jvolgeores.2009.11.008>
- D'Oriano C, Bertagnini A, Pompilio M (2011) Ash erupted during normal activity at Stromboli (Aeolian Islands, Italy) raises questions on how the feeding system works. *Bull Volcanol* 73(5):471–477. <https://doi.org/10.1007/s00445-010-0425-0>
- D'Oriano C, Pompilio M, Bertagnini A, Cioni R, Pichavant M (2013) Effects of experimental reheating of natural basaltic ash at different temperatures and redox conditions. *Contrib Miner Petrol* 165:863–883. <https://doi.org/10.1007/s00410-012-0839-0>
- D'Oriano C, Bertagnini A, Cioni R, Pompilio M (2014) Identifying recycled ash in basaltic eruptions. *Sci Rep* 4(1). <https://doi.org/10.1038/srep05851>
- Deardorff N, Cashman K (2017) Rapid crystallization during recycling of basaltic andesite tephra: timescales determined by reheating experiments. *Sci Rep* 7(1):46364. <https://doi.org/10.1038/srep46364>
- Del Moro S, Renzulli A, Landi P, La Felice S, Rosi M (2013) Unusual lapilli tuff ejecta erupted at Stromboli during the 15 March 2007 explosion shed light on the nature and thermal state of rocks forming the crater system of the volcano. *J Volcanol Geoth Res* 254:37–52. <https://doi.org/10.1016/j.jvolgeores.2012.12.017>

- Sable JE, Houghton BF, Wilson CJN, Carey RJ (2006b) Complex proximal sedimentation from Plinian plumes: the example of Tarawera 1886. *Bull Volcanol* 69(1):89–103. <https://doi.org/10.1007/s00445-006-0057-6>
- Sable JE, Houghton BF, Wilson CJN, Carey RJ (2009) Eruption mechanisms during the climax of the Tarawera 1886 basaltic Plinian eruption inferred from microtextural characteristics of the deposits. In: *Studies in Volcanology: The Legacy of George Walker*. Special Publications of IAVCEI, Geological Society of London, pp 129–153
- Sahagian DL, Proussevitch AA (1998) 3D particle size distributions from 2D observations: stereology for natural applications. *J Volcanol Geoth Res* 84(3):173–196. [https://doi.org/10.1016/S0377-0273\(98\)00043-2](https://doi.org/10.1016/S0377-0273(98)00043-2)
- Schipper C, White J (2016) Magma-slurry interaction in Surtseyan eruptions. *Geology* 44(3):195–198. <https://doi.org/10.1130/G37480.1>
- Shea T, Houghton BF, Gurioli L, Cashman KV, Hammer JE, Hobden BJ (2010) Textural studies of vesicles in volcanic rocks: an integrated methodology. *J Volcanol Geoth Res* 190(3–4):271–289. <https://doi.org/10.1016/j.jvolgeores.2009.12.003>
- Smith SP (1886a) Preliminary report on the volcanic eruption at Tarawera. Appendix J House Representatives 26:1–4
- Smith SP (1886b) The eruption of Tarawera: a report to the Surveyor-General. In: Government Printer, Wellington
- Sparks RSJ (1978) The dynamics of bubble formation and growth in magmas: a review and analysis. *J Volcanol Geoth Res* 3(1):1–37. [https://doi.org/10.1016/0377-0273\(78\)90002-1](https://doi.org/10.1016/0377-0273(78)90002-1)
- Sparks RSJ, Wright JV (1979) Welded air-fall tuffs. In: *Ash-Flow Tuffs*. Geological Society of America
- Stovall WK, Houghton BF, Gonnermann H, Fagents SA, Swanson DA (2011) Eruption dynamics of Hawaiian-style fountains: the case study of episode 1 of the Kīlauea Iki 1959 eruption. *Bull Volcanol* 73(5):511–529. <https://doi.org/10.1007/s00445-010-0426-z>
- Sumner JM (1998) Formation of clastogenic lava flows during fissure eruption and scoria cone collapse: the 1986 eruption of Izu-Oshima Volcano, eastern Japan. *Bull Volcanol* 60(3):195–212. <https://doi.org/10.1007/s004450050227>
- Sumner JM, Branney MJ (2002) The emplacement history of a remarkable heterogeneous, chemically zoned, rheomorphic and locally lava-like ignimbrite: ‘TL’ on Gran Canaria. *J Volcanol Geoth Res* 115(1):109–138. [https://doi.org/10.1016/S0377-0273\(01\)00311-0](https://doi.org/10.1016/S0377-0273(01)00311-0)
- Sumner JM, Blake S, Matela RJ, Wolff JA (2005) Spatter. *J Volcanol Geoth Res* 142(1–2):49–65. <https://doi.org/10.1016/j.jvolgeores.2004.10.013>
- Szramek L, Gardner JE, Hort M (2010) Cooling-induced crystallization of microlite crystals in two basaltic pumice clasts. *Am Miner* 95(4):503–509. <https://doi.org/10.2138/am.2010.3270>
- Taddeucci J, Pompilio M, Scarlato P (2004) Conduit processes during the July–August 2001 explosive activity of Mt Etna (Italy): inferences from glass chemistry and crystal size distribution of ash particles. *J Volcanol Geotherm Res* 137(1):33–54. <https://doi.org/10.1016/j.jvolgeores.2004.05.011>
- Taddeucci J, Cimarelli C, Alatorre-Ibargüenoiitia MA, Delgado-Granados H, Andronico D, Del Bello E, Scarlato P, Di Stefano F (2021) Fracturing and healing of basaltic magmas during explosive volcanic eruptions. *Nat Geosci* 14(4):248–254. <https://doi.org/10.1038/s41561-021-00708-1>
- Tait S, Thomas R, Gardner J, Jaupart C (1998) Constraints on cooling rates and permeabilities of pumice in an explosive eruption jet from colour and magnetic mineralogy. *J Volcanol Geoth Res* 86:79. [https://doi.org/10.1016/S0377-0273\(98\)00075-4](https://doi.org/10.1016/S0377-0273(98)00075-4)
- Thomas RME, Sparks RSJ (1992) Cooling of tephra during fallout from eruption columns. *Bull Volcanol* 54(7):542–553. <https://doi.org/10.1007/BF00569939>
- Walker GPL, Self S, Wilson L (1984) Tarawera 1886, New Zealand — a basaltic plinian fissure eruption. *J Volcanol Geoth Res* 21(1):61–78. [https://doi.org/10.1016/0377-0273\(84\)90016-7](https://doi.org/10.1016/0377-0273(84)90016-7)
- White J, Houghton B (2006) Primary volcanoclastic rocks. *Geology* 34(8):677–680. <https://doi.org/10.1130/G22346.1>
- Williams WL (1887) Phenomena connected with the Tarawera eruption of 10th June as observed at Gisbourne. *Trans Proc R Soc NZ* 19:380–382
- Woodcock DC, Lane SJ, Gilbert JS (2016) Ice-melt rates during volcanic eruptions within water-drained, low-pressure subglacial cavities. *J Geophys Res: Solid Earth* 121(2):648–662. <https://doi.org/10.1002/2015JB012036>
- Xu Z, Zhang Y (2002) Quench rates in air, water, and liquid nitrogen, and inference of temperature in volcanic eruption columns. *Earth Planet Sci Lett* 200(3):315–330. [https://doi.org/10.1016/S0012-821X\(02\)00656-8](https://doi.org/10.1016/S0012-821X(02)00656-8)
- Yamagishi H, Feebrey C (1994) Ballistic ejecta from the 1988–1989 andesitic Vulcanian eruptions of Tokachidake volcano, Japan: morphological features and genesis. *J Volcanol Geoth Res* 59(4):269–278. [https://doi.org/10.1016/0377-0273\(94\)90082-5](https://doi.org/10.1016/0377-0273(94)90082-5)